

# Controllable synthesis of h-WO<sub>3</sub> nanoflakes by L-lysine assisted hydrothermal route and electrochemical characterization of nanoflake-modified glassy carbon electrode

Vijaya Kumar Gangaiah<sup>1</sup>, Ashoka Siddaramanna<sup>2</sup>, Prashanth Shivappa Adarakatti<sup>3</sup>, Gujjarahalli Thimanna Chandrappa<sup>1\*</sup>

<sup>1</sup>Department of Chemistry, Bangalore University, Bengaluru, India

<sup>2</sup>Department of Chemistry, Dayananda Sagar University, Kudlu Gate, Bengaluru, India

<sup>3</sup>Solid State and Structural Chemistry Unit, Indian Institute of Science, Bengaluru, India

\*Correspondence: gtchandrappa@yahoo.co.in

## ABSTRACT

Hexagonal tungsten trioxide (h-WO<sub>3</sub>) nanoflakes have been synthesized by a hydrothermal approach using L-lysine as the shape directing agent. The influence of hydrothermal reaction time and L-lysine content on the morphology of h-WO<sub>3</sub> was investigated. The experimental results showed that the nanoflake morphology could be achieved at higher concentration of L-lysine. Based on the evolution of nanoflake morphology as a function of hydro-thermal duration, a “dissolution-crystallization-Ostwald ripening” growth mechanism has been proposed. The electro-chemical performance of h-WO<sub>3</sub> nanoflakes has also been investigated by cyclic voltammetry (CV) and electrochemical impedance spectroscopy (EIS). It is found that h-WO<sub>3</sub> modified glassy carbon electrode (GCE) showed lower charge transfer resistance and enhancement in peak current attributed to the enrichment in electroactive surface area and faster electron transfer kinetics at h-WO<sub>3</sub> modified GCE.

**Keywords:** heat transfer. Hydrothermal; Nanoflakes; Morphology; Cyclic voltammogram; Electrochemical Impedance

**Received:** Nov 17, 2021    **Accepted:** Dec 21, 2021    **Online:** Jan 9, 2022

## 1. Introduction

Tungsten trioxide (WO<sub>3</sub>) is one of the most investigated functional metal oxides with widespread applications. It exhibits distinctive electrochromic, photochromic, field emission, photocatalytic, and sensing properties, which endow it a potential candidate in technological applications such as smart window devices<sup>[1,2]</sup>, dye-sensitized solar cells<sup>[3,4]</sup>, water splitting applications<sup>[5,6]</sup>, field emission devices<sup>[7,8]</sup>, photocatalysts<sup>[9,10]</sup>, and gas sensors<sup>[11,12]</sup>.

WO<sub>3</sub> is an indirect n-type wide band gap (~2-8 eV) oxide semiconductor material<sup>[13]</sup>. WO<sub>3</sub> exists in six polymorphs: h-WO<sub>3</sub> (hexagonal structure), β-WO<sub>3</sub> (orthorhombic structure), α-WO<sub>3</sub> (tetragonal structure), δ-WO<sub>3</sub> (triclinic structure), γ-WO<sub>3</sub> (monoclinic structure), and ε-WO<sub>3</sub> (monoclinic structure). These polymorphs are usually formed by corner and edge sharing of WO<sub>6</sub> octahedral units<sup>[14]</sup>.

There have been significant efforts focused on controlling the morphology and microstructure of WO<sub>3</sub>, which facilitates to tune and optimize properties of the material. Hydrothermal approach is one of the well-known solution phase synthetic routes to prepare WO<sub>3</sub> nanostructures, which offers precise control over the size and shape of the final product<sup>[15,16]</sup>. Numerous hydrothermal routes have been reported for synthesizing diverse nanostructures of WO<sub>3</sub> including nanorods<sup>[17]</sup>, nanowires<sup>[18]</sup>, nanobelts<sup>[19]</sup>, nanoplates<sup>[20]</sup>, nanocrystals<sup>[21]</sup>, and hierarchical structures<sup>[22]</sup>.

There have been few synthesis efforts focusing on amino acid assisted hydrothermal routes for preparing metal oxide nanostructures, in which amino acids act as shape directing agents<sup>[23-28]</sup>. For instance, Wu et al. reported the synthesis of

ZnO hierarchical architectures via hydrothermal method at a temperature of 150 °C for 15 hours using the amino acid histidine as the shape directing agent<sup>[23]</sup>. Liang et al. prepared MoO<sub>3</sub> nanowires through aspartic acid assisted hydrothermal synthesis<sup>[24]</sup>. Zheng et al. synthesized ZrO<sub>2</sub> nanocrystals with narrow size distribution through hydrothermal route using L-lysine at a selected temperature ranging from 170 to 260 °C <sup>[25]</sup>. Wu et al. reported the lysine-assisted hydrothermal synthesis of SnO<sub>2</sub> nanocrystals with controllable size and shape<sup>[26]</sup>. Herein, we report L-lysine assisted hydrothermal route to prepare h-WO<sub>3</sub> with nanoflake morphologies. The possible growth mechanism is proposed for the formation of h-WO<sub>3</sub> nanoflakes on the basis of time dependent hydrothermal experiments. The electrochemical activity of h-WO<sub>3</sub> nanoflakes has been investigated by utilizing them in electrochemical modification of glassy carbon electrode.

## 2. Experimental section

### 2.1 Synthesis of h-WO<sub>3</sub> nanoflakes

In a typical synthesis, 1 mM of sodium tungstate dihydrate (Na<sub>2</sub>WO<sub>4</sub>·2H<sub>2</sub>O) and 5 mM of L-lysine (C<sub>6</sub>H<sub>14</sub>N<sub>2</sub>O<sub>2</sub>) were dissolved separately in 20 mL distilled water, and mixed together. The resulting solution was subjected to gentle stirring for 30 minutes and then acidified to pH 1.0 using 4M HCl solution. Finally, the obtained mixture was transferred into a Teflon-lined stainless-steel autoclave of 60 mL capacity and subjected to hydrothermal treatment (180 °C, 12 h). After cooling down to room temperature, the products were collected by centrifugation and subsequently washed with distilled water and ethanol for several times. Finally, the products were dried in air at 70 °C for 10 h.

### 2.2 Characterization

The identification of the phase was examined by Panalytical XPert Pro MPD powder X-ray diffractometer (PXRD) using Cu-K $\alpha$  radiation at ( $\lambda=1.5418$  Å) at in the 2 $\theta$  range between 10 and 60 °C. Scanning electron microscopy (SEM) observation and energy dispersive X-ray (EDX) analysis were performed on VEGA3 TESCAN scanning electron microscope. Transmission electron microscopy (TEM), high-resolution TEM (HR-TEM) images and the analogous selected area electron diffraction (SAED) patterns were taken on a JEOL JEM-2100 transmission electron microscope. The X-ray photoelectron spectroscopy (XPS) analysis was carried out on a ThermoFisher Scientific ESCLAB-250 X-ray photoelectron spectrometer using Al-K $\alpha$  monochromatic X-ray radiation. Fourier transform Infrared (FTIR) spectrum was recorded over the range of 4000 to 400 cm<sup>-1</sup> with a NiCOLET 380 FTIR spectrometer with the product in a KBr pellet. Electrochemical measurements were carried out at room temperature using CH Instruments (model: CHI 619B) electrochemical work station. A modified glassy carbon electrode was used as the working electrode, a platinum wire served as the counter electrode and Ag/AgCl as the reference electrode.

### 2.3 Electrode modification

The GCE was polished with 0.3 and 0.05  $\mu$ m alumina particles to obtain a mirror smooth surface. The polished GCE was washed thoroughly with double distilled water using ultrasonic bath followed by rinsed with ethanol and then dried at room temperature. 10 mg of as synthesized h-WO<sub>3</sub> nanoflakes were dispersed in 10 mL of distilled water using ultrasonic bath. Then, the obtained dispersed suspension (of volume 5  $\mu$ L) was drop casted on to the GCE and subsequently dried it in vacuum at room temperature.

## 3. Results and discussion

### 3.1 h-WO<sub>3</sub> nanoflakes

The phase and the morphology of the hydrothermally derived product at 180 °C for 12 h in the presence of 5 mM of L-lysine were investigated by PXRD and SEM techniques. As observed in the PXRD pattern of the product (**Figure 1**), the diffraction peaks can be readily indexed to hexagonal phase of WO<sub>3</sub> (h-WO<sub>3</sub>) (JCPDS 33-1387). No apparent peaks of other phases of WO<sub>3</sub> are observed. **Figure 2** depicts the SEM image of the hydrothermally derived product, which reveals that the product consists of stacked nanoflakes. The morphology and structural features of the product were further studied by TEM and HRTEM as shown in **Figure 3**. **Figure 3a** shows the high magnification TEM image of the hydrothermally derived product at 180 °C for 12 h in the presence of 5 mM of L-lysine, which reveals that the product consists of stacked nanoflakes of irregular shapes.

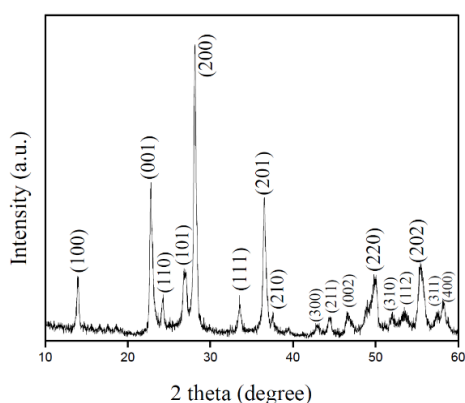


**Figure 1.** PXRD pattern of the hydrothermally derived product at 180 °C for 12 h in the presence of 5 mM of L-lysine.

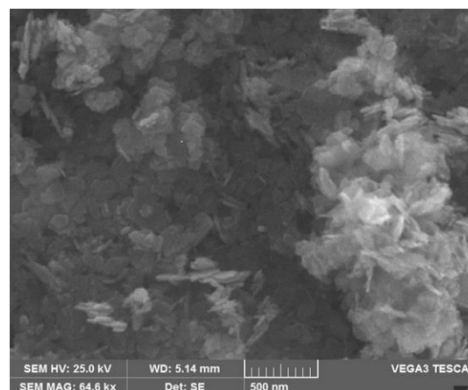


**Figure 2.** SEM image of the hydrothermally derived product at 180 °C for 12 h in the presence of 5 mM L-lysine.

As observed from the TEM image, lateral dimensions of the nanoflakes are in the range of 50 - 80 nm and thickness is in the nanometer range. HRTEM (**Figure 3b**) and SAED (**Figure 3c**) results show that the h-WO<sub>3</sub> nanoflakes are single crystalline in nature. The SAED pattern recorded perpendicular to the growth axes of a typical nanoflake could be attributed to the diffraction of [010] zone axis of h-WO<sub>3</sub>. From the HRTEM image, it can be measured that the interplanar spacing of 0.386 nm corresponds to lattice spacing of (002) of hexagonal phase of WO<sub>3</sub>.

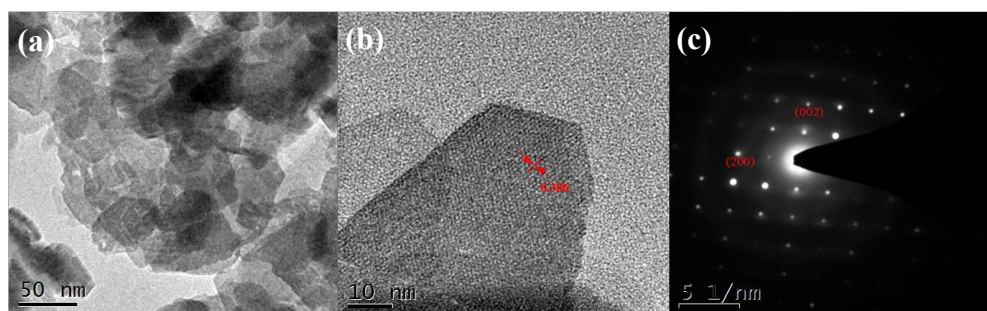


**Figure 3.** High magnification TEM image of (a) h-WO<sub>3</sub> nanoflakes (b) representative HRTEM image of a nanoflake, and (c) corresponding SAED pattern.

In addition to phase identification of the product as h-WO<sub>3</sub> by PXRD analysis, the chemical composition of the product was investigated by energy-dispersive X-ray (EDX) spectroscopy and XPS techniques. **Figure 4** displays the EDX spectrum of h-WO<sub>3</sub> nanoflakes. As observed in the EDX spectrum, the product is composed of W and O elements, and the molar ratio of W:O is determined to be 1:3. **Figure 5a** illustrates the XPS survey spectrum of h-WO<sub>3</sub> nanoflakes, in which peaks of W 4f, W 4d, W 4p, O 1s, and C 1s can be observed. The XPS spectrum (**Figure 5b**) of W 4f region shows two strong peaks at 35.9 eV and 38.1 eV, which are attributed to binding energies of W 4f<sub>7/2</sub> and W 4f<sub>5/2</sub> of W<sup>6+</sup> ions in WO<sub>3</sub>. **Figure 5c** depicts the XPS spectrum of O 1s region which shows only a single peak centered at 530.7 eV which can be assigned to lattice oxygen in WO<sub>3</sub> [29].

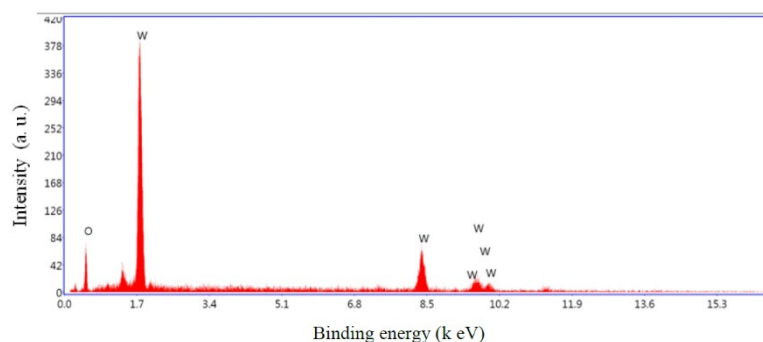


**Figure 4.** EDX spectrum of h-WO<sub>3</sub> nanoflakes.

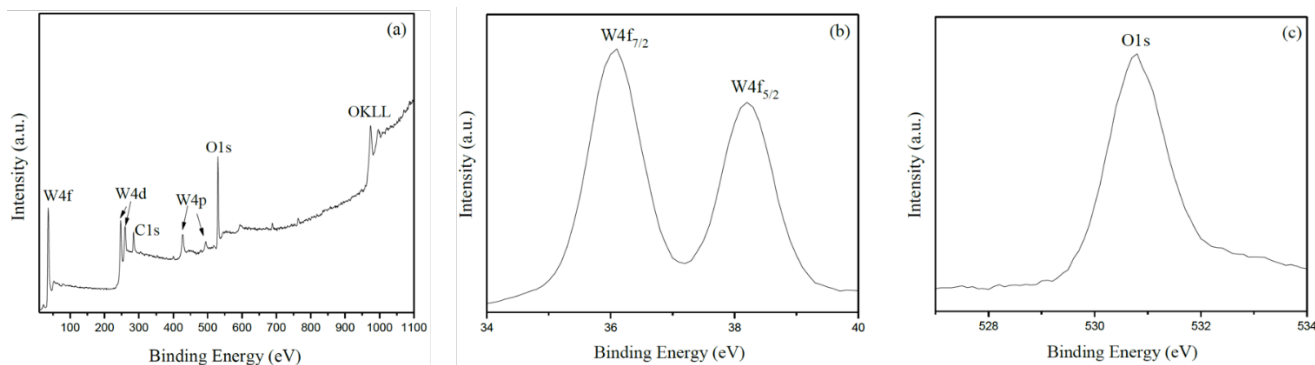


**Figure 5.** (a) XPS survey spectrum of h-WO<sub>3</sub> nanoflakes; (b) XPS spectrum of the W 4f region; (c) XPS spectrum of the O 1s region.

FTIR analysis was carried out to investigate the states of chemical bonding between molybdenum and oxygen atoms in the h-WO<sub>3</sub> nanoflakes. **Figure 6** depicts the FTIR spectrum of h-WO<sub>3</sub> nanoflakes measured over the range of 4000-400 cm<sup>-1</sup>. The broad absorption band observed between 500 and 1000 cm<sup>-1</sup> can be attributed to vibrational modes of O-W-O-W and W-O linkages<sup>[30]</sup>. The broad absorption band with a maximum at 3467 cm<sup>-1</sup> and the obvious absorption band at 1615 cm<sup>-1</sup> are assignable as O-H stretching and bending vibrations of adsorbed water molecules, respectively.

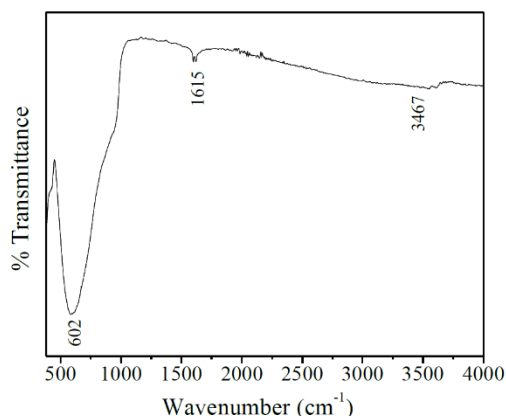


**Figure 6.** FTIR spectrum of the as synthesized h-WO<sub>3</sub> nanoflakes.

To investigate the effect of L-lysine on the morphology of h-WO<sub>3</sub>, hydrothermal experiments were carried out by varying the amount of L-lysine while keeping other experimental parameters unaltered. **Figure 7a** and **Figure 7b** show the SEM images of the synthesized products with 2 mM of L-lysine and in the absence of L-lysine, respectively. As shown in **Figure 7a**, aggregated square plate-like structures with larger sizes were observed for 2 mM of L-lysine compared with morphology observed at 5 mM of L-lysine. In the absence of L-lysine, irregular microstructural aggregations were observed (**Figure 7b**). From these results, it is evident that the amount of L-lysine significantly affects the morphology of the hydrothermally derived product, and that nanoflake like structures should only be obtained under 5 mM of L-lysine.

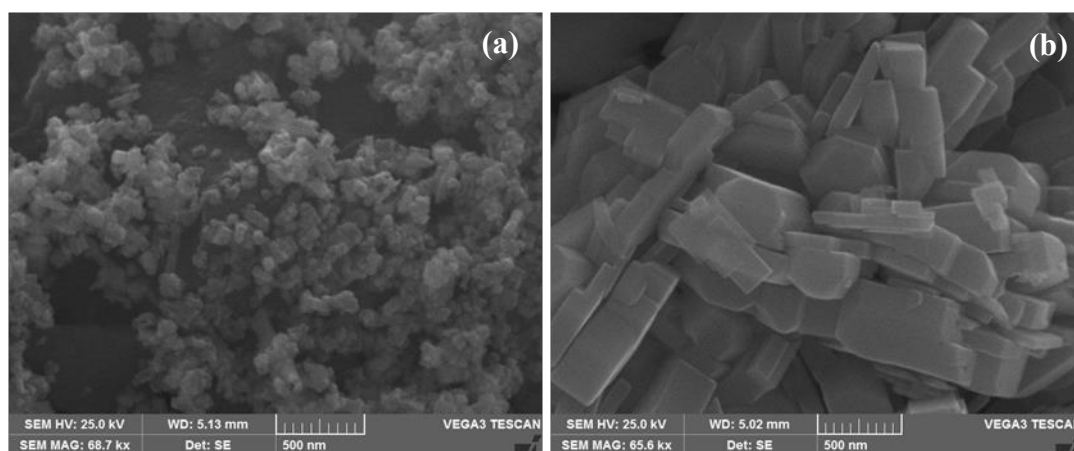


**Figure 7.** SEM images of the hydrothermally derived products: (a) with 2 mM of L-lysine and (b) in the absence of L-lysine.

In order to reveal the formation process of h-WO<sub>3</sub> nanoflakes, time dependent hydrothermal experiments were performed at 180 °C for time intervals of 2 h, 6 h, and 8 h in the presence of 5 mM of L-lysine. The PXRD patterns and the SEM images of intermediate products obtained at 2 h, 6 h, and 8 h are displayed in **Figure 8** and **Figure 9**, respectively. After hydrothermal treatment for 2 h, it is observed that the product was amorphous (**Figure 8a**) in nature with the morphology of microspheres (**Figure 9a**). On proceeding the hydrothermal treatment to 6 h, characteristic peaks of the hexagonal phase of WO<sub>3</sub> (**Figure 8a**) appeared. The corresponding SEM image is shown in **Figure 9b**, where flake-like structures in microscopic aggregations were observed. After the hydrothermal treatment extended for 8 h, diffraction peaks of h-WO<sub>3</sub> (**Figure 8c**) became obvious with the morphology of stacked nanoflake structures (**Figure 9c**).

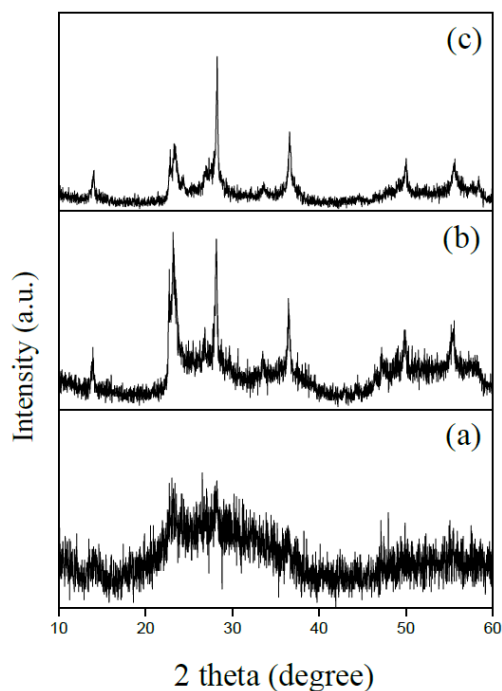


**Figure 8.** PXRD patterns of the intermediate products collected at different hydrothermal reaction time intervals: (a) 2 h, (b) 6 h and (c) 8 h

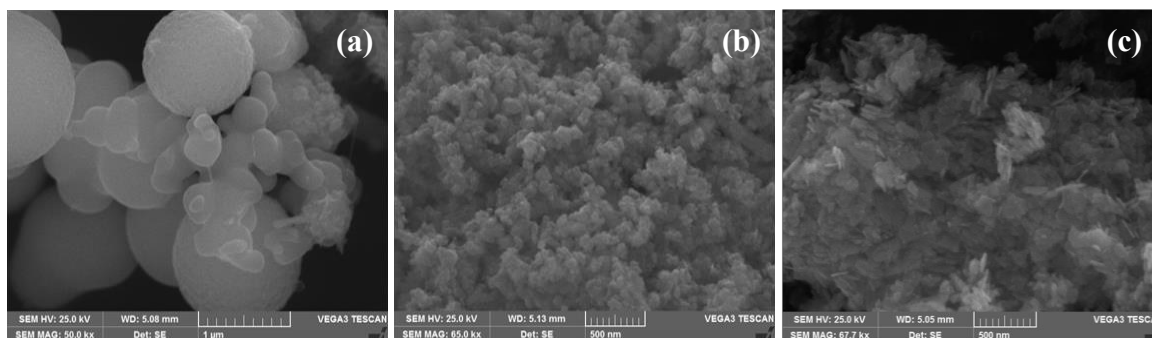
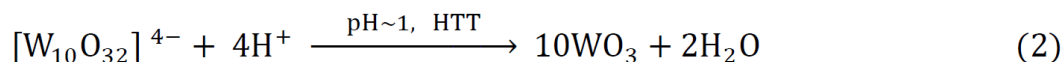
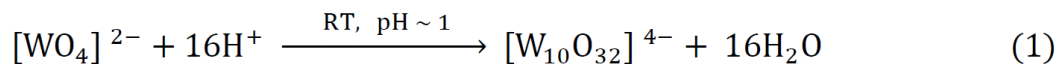


**Figure 9.** SEM images of the intermediate products collected at different hydrothermal durations: (a) 2 h, (b) 6 h and (c) 8 h.

Based on the above time dependent experimental results, the formation process of h-WO<sub>3</sub> nanoflake structures can be explained as follows: In the initial stage, the amorphous microspheres are formed and get dissolved on prolonging the hydrothermal reaction. On further proceeding the reaction, crystallization begins with nucleation of WO<sub>3</sub> crystallites. These crystallites tend to self-assemble into small flake-like structures as a result of reduction in the surface energy of crystallites. The self-assembly of WO<sub>3</sub> crystallites are directed under the influence of L-lysine. In the present work, L-lysine serves as structure directing agent, which results in the formation of nanoflake like structures. L-lysine is an amino acid (C<sub>6</sub>H<sub>14</sub>N<sub>2</sub>O<sub>2</sub>: NH<sub>2</sub>-CH<sub>2</sub>-CH<sub>2</sub>-CH<sub>2</sub>-CH<sub>2</sub>-CH(NH<sub>2</sub>)-COOH) with one carboxylic group and two amino groups. During the growth process, under the influence of L-lysine, crystallites prefer to grow into flake-like structures. The small flake-like structures grow gradually via Ostwald ripening, leading to the formation of independent larger nanoflakes. L-lysine molecules may be adsorbed preferentially on to the (010) plane of WO<sub>3</sub>, thereby inhibiting the growth along [010] direction. This results in the preferential growth of the nanoflake structure along [100] and [001] directions. The whole growth mechanism can be designated as “Dissolution-crystallization-Ostwald ripening”. The possible chemical reactions for the formation of h-WO<sub>3</sub> can be expressed as follows:



Prior to the hydrothermal treatment, when the pH of the reaction solution was reduced to  $\sim 1.0$ , tungstate ion undergoes dehydration by  $\text{H}^+$  ions, followed by condensation to form  $[\text{W}_{10}\text{O}_{32}]^{4-}$  polytungstate ions<sup>[31,32]</sup> as shown in equation (1). At this pH, L-lysine is positively charged in the reaction solution because its acid dissociation constant ( $\text{pK}_a \text{COOH}$ ) is 2.2<sup>[33]</sup>. L-lysine therefore serves as a counter cation to  $[\text{W}_{10}\text{O}_{32}]^{4-}$  ion in the reaction solution. The hydrothermal treatment of the reaction solution containing  $[\text{W}_{10}\text{O}_{32}]^{4-}$  ions leads to  $\text{WO}_3$  as shown in equation (2).

## 3.2 Electrochemical characterization

Electrochemical performance of h- $\text{WO}_3$  nanoflakes has been investigated using cyclic voltammetry (CV) and electrochemical impedance spectroscopy (EIS). To investigate the electrochemical properties of h- $\text{WO}_3$  modified glassy carbon electrode (GCE),  $[\text{Fe}(\text{CN})_6]^{3-/4-}$  is used as an electrochemical probe. The cyclic voltammograms of bare and h- $\text{WO}_3$  modified GCE in 0.1M KCl solution as supporting electrolyte containing 5 mM  $[\text{Fe}(\text{CN})_6]^{3-/4-}$  at a scan rate of 50 mV/s are shown in the **Figure 10a** and **Figure 10b** respectively. A pair of well-defined reversible redox peaks were observed for both bare and h- $\text{WO}_3$  modified GCE. As compared to the bare, h- $\text{WO}_3$  modified GCE showed enhancement in peak current and minimization in peak potential which may be attributed to the enrichment in electroactive surface area of the modified electrode and thereby stimulates the electron transfer to takes place rapidly between the bulk solution and the modified electrode.

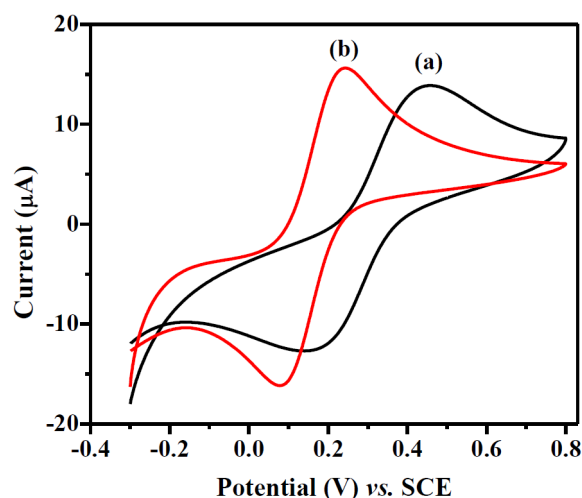


**Figure 10.** Cyclic voltammograms of (a) bare and (b) h- $\text{WO}_3$  modified GCE in 0.1 M KCl solution containing 5 mM  $[\text{Fe}(\text{CN})_6]^{3-/4-}$  at a scan rate of 50 mV/s.

EIS study was carried out to understand the feasibility of electrons across the interface of surface modified electrode. **Figure 11a** and **Figure 11b** represent the Nyquist plots of 5 mM  $[\text{Fe}(\text{CN})_6]^{3-/4-}$  containing 0.01 M KCl on bare and h- $\text{WO}_3$  modified GCE, respectively. The obtained impedance data was fitted with Randles electrical circuit as shown in the inset of **Figure 11** where  $C_{dl}$ ,  $R_s$ ,  $R_{ct}$ , and  $Z_W$  represent the double layer capacitance, electrolyte resistance, charge transfer resistance, and Warburg impedance, respectively. In the Nyquist plots, the presence of semicircle at high frequency region indicates the electron transfer limited process and the linear part at low frequency region indicates the diffusion limited process<sup>[34]</sup>. The diameter of the semicircle represents the charge transfer resistance ( $R_{ct}$ ) of the electrode.  $R_{ct}$  for bare GCE and h- $\text{WO}_3$  modified GCE was found to be 3.254 and 0.959 k $\Omega$ , respectively. As compared to bare GCE, the magnitude of charge transfer resistance greatly decreased with the modification of h- $\text{WO}_3$  on GCE, which might be attributed to large surface area, high conductivity and faster electron transfer kinetics at h- $\text{WO}_3$  modified GCE.

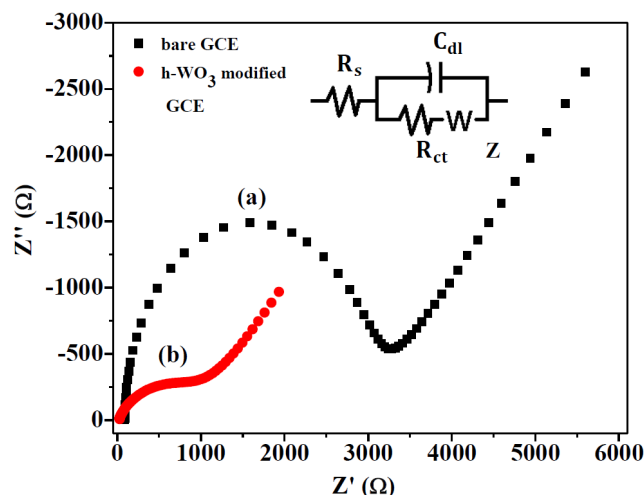


**Figure 11.** Nyquist plots of (a) bare GCE and (b) h-WO<sub>3</sub> modified GCE in 10 mM KCl containing 5 mM [Fe(CN)<sub>6</sub>]<sup>3-/4-</sup>; Inset: Randles equivalent circuit model.

## 4. Conclusions

In summary, we have reported the controllable synthesis of h-WO<sub>3</sub> nanoflakes through L-lysine-assisted hydro-thermal route. It was found that the nanoflake morphology could be achieved at higher concentration of L-lysine. A “dissolution-crystallization-Ostwald ripening” growth mechanism has been proposed on the basis of morphological evolution of nanoflake as a function of hydrothermal time. The electrochemical performance of h-WO<sub>3</sub> nanoflakes has been investigated by utilizing them as electrochemical modifiers for GCE. h-WO<sub>3</sub> modified GCE showed lower charge transfer resistance and enhancement in peak current attributed to the enhancement in electroactive surface area and faster electron transfer kinetics at modified electrode. Therefore, h-WO<sub>3</sub> nanoflakes modified GCE may find possible applications in metal ions and biomolecules sensors.

## Acknowledgement

GTC thanks the Department of Science and Technology (DST), Nano Mission, New Delhi, India, for financial support.

## References

1. More AJ, Patil RS, Dalavi DS, et al. Synthesis and characterization of potentiostatically electrodeposited tungsten oxide thin films for smart window application. *Journal of Electronic Materials*, 2017, 46 (2): 974-981.
2. Park S, Kim S, Choi JO, et al. Low-cost fabrication of WO<sub>3</sub> films using a room temperature and low-vacuum air-spray based deposition system for inorganic electrochromic device applications. *Thin Solid Films*, 2015, 589: 412-418.
3. Zheng H, Tachibana Y, Zadeh KK. Dye-Sensitized Solar Cells Based on WO<sub>3</sub>. *Langmuir*, 2010, 26 (24): 19148-19152.
4. Hara K, Zhao ZG, Cui Y, et al. Nanocrystalline electrodes based on nanoporous-walled WO<sub>3</sub> nanotubes for organic-dye sensitized solar cells. *Langmuir*, 2011, 27: 12730-12736.
5. Liu X, Wang F, Wang Q. Nanostructure-based WO<sub>3</sub> photoanodes for photoelectrochemical water splitting. *Physical Chemistry Chemical Physics*, 2012, 14: 7894-7911.
6. Rao PM, Cho IS, Zheng X. Flame synthesis of WO<sub>3</sub> nanotubes and nanowires for efficient photoelectrochemical water-splitting. *Proceedings of the Combustion Institute*, 2013, 34 (2): 2187-2195.
7. Chang MT, Chou LJ, Chueh YL, et al. Nitrogen-doped tungsten oxide nanowires: low-temperature synthesis on Si, and electrical, optical, and field-emission properties. *Small*, 2007, 3 (4): 658664.
8. Trapatseli M, Vernardou D, Tzanetakis P, et al. Field emission properties of low-temperature, hydrothermally grown tungsten oxide. *ACS Applied Materials and Interfaces*, 2011, 3 (7) : 2726-2731.
9. Aslama M, Ismai IMI, Chandrasekaran S, et al. Morphology controlled bulk synthesis of disc-shaped WO<sub>3</sub> powder and evaluation of its photocatalytic activity for the degradation of phenols. *Journal of Hazardous Materials*, 2014, 276: 120-128.
10. Fujii A, Meng Z, Yogi C, et al. Preparation of Pt-loaded WO<sub>3</sub> with different types of morphology and photocatalytic degradation of methylene blue. *Surface and Coatings Technology*, 2015, 271: 251-258.
11. Wang Z, Hu M, Wei Y, et al. Low-temperature NO<sub>2</sub>-sensing properties and morphology-controllable solvothermal synthesis of tungsten oxide nanosheets/nanorods. *Applied Surface Science*, 2016, 362: 525-531.

12. Meng Z, Fujii A, Hashishin T, et al. Morphological and crystal structural control of tungsten trioxide for highly sensitive NO<sub>2</sub> gas sensors. *Journal of Materials Chemistry C*, 2015, 3 (4): 1134-1141.
13. Cong S, Geng F, Zhao Z, et al. Tungsten Oxide Materials for Optoelectronic Applications. *Advanced Materials*, 2016, 28 (47): 10518-10528.
14. Ramana CV, Utsunomiya S, Ewing RC, et al. Structural stability and phase transitions in WO<sub>3</sub> thin films. *Journal of Physical Chemistry B*, 2006, 110 (21): 10430-10435.
15. Zheng H, Ou JZ, Strano MS, et al. Nanostructured tungsten oxide -Properties, synthesis, and applications. *Advanced Functional Materials*, 2011, 21 (12): 2175-2196.
16. Bai S, Zhang K, Luo R, et al. Low-temperature hydrothermal synthesis of WO<sub>3</sub> nanorods and their sensing properties for NO<sub>2</sub>. *Journal of Materials Chemistry*, 2012, 22 (25): 12643-12650.
17. Salmaoui S, Sediri F, Gharbi N. Characterization of h-WO<sub>3</sub> nanorods synthesized by hydrothermal process. *Polyhedron*, 2010, 29 (7): 1771-1775.
18. Navarro JRG, Mayence A, Andrade J, et al. WO<sub>3</sub> nanorods created by self-assembly of highly crystalline nanowires under hydrothermal conditions. *Langmuir*, 2014, 30 (34): 10487-10492.
19. Song X, Zhao Y, Zheng Y. Hydrothermal synthesis of tungsten oxide nanobelts. *Materials Letters*, 2006, 60 (28): 3405-3408.
20. Gao X, Su X, Yang C, et al. Hydrothermal synthesis of WO<sub>3</sub> nanoplates as highly sensitive cyclohexene sensor and high-efficiency MB photocatalyst. *Sensors and Actuators B: Chemical*, 2013, 181: 537-543.
21. Pang HF, Xiang X, Li ZJ, et al. Hydrothermal synthesis and optical properties of hexagonal tungsten oxide nanocrystals assisted by ammonium tartrate. *Physica Status Solidi A*, 2012, 209 (3): 537-544.
22. Wang J, Lee PS, Ma J. One-pot synthesis of hierarchically assembled tungsten oxide (hydrates) nano/microstructures by a crystal-seed-assisted hydrothermal process. *Crystal Growth and Design*, 2009, 9 (5): 2293-2299.
23. Wu Q, Chen X, Zhang P, et al. Amino acid-assisted synthesis of zno-hierarchical architectures and their novel photocatalytic activities. *Crystal Growth and Design*, 2008, 8 (8): 3010-3018.
24. Liang R, Cao H, Qian D. MoO<sub>3</sub> nanowires as electrochemical pseudocapacitor materials *Chemical Communications*, 2011, 47 (37): 10305-10307.
25. Zheng H, Liu K, Cao H, et al. L-lysine-Assisted Synthesis of ZrO<sub>2</sub> Nanocrystals and Their Application in Photocatalysis. *Journal of Physical Chemistry C*, 2009, 113 (42): 18259-18263.
26. Wu S, Cao H, Yin S, et al. Amino acid-assisted hydrothermal synthesis and photocatalysis of SnO<sub>2</sub> nanocrystals. *Journal of Physical Chemistry C*, 2009, 113 (41): 17893-17898.
27. Tao Y, Cao N, Pan J, et al. Controllable synthesis of TiO<sub>2</sub> nanomaterials by assisting with L-cysteine and ethylenediamine. *Journal of Material Science*, 2014, 49 (2): 897-904.
28. Zhang J, Sun Y, Yao Y, et al. Lysine-assisted hydrothermal synthesis of hierarchically porous Fe<sub>2</sub>O<sub>3</sub> microspheres as anode materials for lithium-ion batteries. *Journal of Power Sources*, 2013, 222: 59-65.
29. Wu H, Xu M, Da P, et al. WO<sub>3</sub>-reduced graphene oxide composites with enhanced charge transfer for photoelectrochemical conversion. *Physical Chemistry Chemical Physics*, 2013, 15 (38): 16138-16142.
30. Chemseddine A, Babonneau F, Livage J. Anisotropic WO<sub>3</sub>·nH<sub>2</sub>O layers deposited from gels. *Journal of Non-Crystalline Solids*, 1987, 91 (2): 271-278.
31. Livage J, Henry M, Sanchez C. Sol-gel chemistry of transition metal oxides. *Progress in Solid State Chemistry*, 1988, 18 (4): 259-341.
32. Chemseddine A, Bloeck U. How isopolyanions self-assemble and condense into a 2D tungsten oxide crystal: HRTEM imaging of atomic arrangement in an intermediate new hexagonal phase. *Journal of Solid-State Chemistry*, 2008, 181 (10): 2731-2736.
33. Ogi T, Makino T, Nagai S, et al. Facile and efficient removal of tungsten anions using lysine-promoted precipitation for recycling high-purity tungsten. *ACS Sustainable Chemistry and Engineering*, 2017, 5 (4): 3141-3147.
34. Oularbi L, Turmine M, Rhazi M E. Electrochemical determination of traces lead ions using a new nanocomposite of polypyrrole/carbon nanofibers. *Journal of Solid-State Electrochemistry*, 2017, 21 (11): 3289-3300.